

# Radio structure and variability of the extreme blazar AO 0235+164

A. M. Kutkin<sup>1\*</sup>, I. N. Pashchenko<sup>1</sup>, M. M. Lisakov<sup>1</sup>, P. A. Voytsik<sup>1</sup>, K. V. Sokolovsky<sup>1,2,3</sup>, Y. Y. Kovalev<sup>1,4</sup>, A. P. Lobanov<sup>4</sup>, A. V. Ipatov<sup>5</sup>, M. F. Aller<sup>6</sup>, H. D. Aller<sup>6</sup>, A. Lahteenmaki<sup>7,8</sup>, et al.

<sup>1</sup>*Astro Space Center of Lebedev Physical Institute, Profsoyuznaya Str. 84/32, 117997 Moscow, Russia*

<sup>2</sup>*Sternberg Astronomical Institute, Moscow State University, Universitetskii pr. 13, 119992 Moscow, Russia*

<sup>3</sup>*IAASARS, National Observatory of Athens, Vas. Pavlou & I. Metaxa, 15236 Penteli, Greece*

<sup>4</sup>*Max-Planck-Institut für RadioAstronomie, Auf dem Hügel 69, D-53121 Bonn, Germany*

<sup>5</sup>*Institute of Applied Astronomy of the Russian Academy of Sciences, 191187, Kutuzov embankment, 10, St. Petersburg, Russia*

<sup>6</sup>*University of Michigan, Astronomy Department, Ann Arbor, MI 48109-1042 USA*

<sup>7</sup>*Aalto University Metsähovi Radio Observatory, 114, Kylmälä, 02540, Finland*

<sup>8</sup>*Department of Radio Science and Engineering, 13000, FI-00076 AALTO, Finland*

Accepted 2017 XXXXX XX. Received 2017 XXXXX XX; in original form 2017 XXXXX XX

## ABSTRACT

Clues on physical conditions in radio cores of blazars come from measurements of brightness temperatures as well as effects produced by intrinsic opacity. We study the properties of ultra compact blazar AO 0235+164 with multi-frequency Space+VLBI and single-dish radio observations. We employ visibility modeling and image stacking for deriving structure and kinematics of the source, and use Gaussian process regression to find relative multi-band time delays of the flares. The apparent core size at cm/mm wavelengths depends on frequency as  $W = \nu^{-0.8 \pm 0.1}$  implying the photosphere interpretation of the core with prevailing synchrotron self absorption. Variability time delays agree with this scenario, but the power index differs significantly for individual flares. The intrinsic brightness temperature in the core is close to equipartition regime value. The jet has moderate Doppler and Lorentz factors  $\delta = 21$ ,  $\Gamma = 14$ . However, there is an evidence for compact regions in the jet with much higher Lorentz and Doppler factors. They might be responsible for the extreme apparent brightness temperatures  $T_b > 10^{13}$  K measured by RadioAstron. In 2007–2016 the VLBI components in the source at 43 GHz are distributed predominantly in two directions. Brighter and more compact reside to the south, while fainter and larger are to the north of the core. We suggest that this structure is caused by the bent of the outflow from southern to northern direction. The apparent opening angle of the jet seen in stacked image at 7 mm  $\varphi = 60^\circ$  is two times higher than one measured by MOJAVE at 2 cm, implying a collimation of the flow within central 1.5 mas. Intrinsic opening angle  $\varphi_{int} = 2^\circ$  is close to the viewing angle of the jet  $\theta = 1.7^\circ$ . The core at 7 mm is about ten parsecs downstream the jet and has magnetic field strength  $B \approx 0.08$  G.

**Key words:** galaxies: active – galaxies: BL Lac – individual – 0235+164: jets – radio continuum: jets – core shift: jets – variability time lags

## 1 INTRODUCTION

Blazars are jetted active galactic nuclei (AGN) viewed at a small angle to the line of sight. They appear on very long baseline interferometry (VLBI) images as unresolved or barely resolved bright core often accompanied by one-sided

jet. Radio emission is produced via synchrotron mechanism and is boosted by relativistic effects. The core has a flat or inverted spectrum at cm-mm wavelengths and is usually interpreted as a unit optical depth jet surface (Blandford & Königl 1979), while alternative interpretations exist (Marscher 2006, 2008). Strong support for the former interpretation comes from the shift between the apparent core positions measured on different frequencies, first detected by

\* E-mail:kutkin@asc.rssi.ru

Marcaide & Shapiro (1984). In the framework of this model, the measured core shift probes jet physics in the core region including magnetic field strength and its distribution along the outflow, linear scales of the jet, its kinetic energy, etc... (Lobanov 1998, Hirotani 2005).

Core shift can be measured directly when a source has prominent jet, so that one can use its optically thin features as a reference or perform a cross-correlation of the maps at different frequencies. There is also an astrometrical way to measure core shift using nearby sources for reference. For a compact source, which does not have a prominent jet, the core shift can be estimated indirectly. If change of the core size measured at different frequencies is due to intrinsic opacity, it can be linked to the core shift the source. Multi-frequency time lags between light curves likely also reflect the offset between the core at two bands and outflow velocity (Kudryavtseva et al. 2011, Kutkin et al. 2014).

The radio source AO 0235+164 (02:38:38.930107 +16:36:59.27460<sup>1</sup>, J2000) was classified as a BL Lac-type object by Spinrad & Smith (1975) on the basis of its variability and optical spectrum that appeared featureless at low spectral resolution (Véron-Cetty & Véron 2010 classify the object as QSO based on its absolute magnitude). Cohen et al. (1987) measured the object's redshift detecting Mg II, [Ne V] and [O II] lines at  $z = 0.94$ . They also found intervening absorption and emission features at lower redshifts. The blazar resides in a field of many faint foreground galaxies (Burbidge et al. 1996, Nilsson et al. 1996) with  $z \sim 0.5$ , and often considered to be affected by gravitational lensing Stickel et al. (1988), Abraham et al. (1993), Webb et al. (2000).

As seen by VLBI, the extended structure in the source is very unstable. Sometimes, it is not detected Gabuzda & Cawthorne (2000), other times there are components at different position angles and various VLBI scales (Jones et al. 1984, Chu et al. 1996). Jorstad et al. (2001) reported jet northwest of the core seen by 7mm VLBA. Later VLBA monitoring revealed the temporary occurrence of a component located south-southeast of the core (Agudo et al. 2011, this paper).

AO 0235+164 demonstrates violent variability across the electromagnetic spectrum on timescales from hours to years. The observed cm-wavelength flux density increases up to 7 times during flaring states. Moreover, there is a strong intra-day variability in the source, which may have intrinsic nature (Qian et al. 2000, Romero et al. 2000).

0235+164 is one of the few most bright sources detected by VSOP and RadioAstron space-VLBI missions on the longest baselines. Its brightness temperature is reported to reach  $T_b \approx 10^{13.8}$  K (Frey et al. 2000), which challenges the inverse Compton limit even after being corrected for boosting with extreme Doppler factor 100.

In this paper we analyze both VLBI (including Space-VLBI RadioAstron data) and single-dish total flux radio observations of blazar 0235+164 in order to shed some light on structure and variability of this enigmatic source.

Observations are summarized in section 2. In §§ 3-4 we describe the methods used for VLBI-data and light curves analysis. Multi-frequency time lags and core size are dis-

cussed in §§ 5-6. Section 7 contains derivation of brightness temperature and Doppler factor as well as RadioAstron measurements. In § 8 we discuss jet structure and estimate its physical and geometrical parameters.

We adopt the standard  $\Lambda$ CDM cosmology model with  $H_0 = 71 \text{ km s}^{-1} \text{ Mpc}^{-1}$ ,  $\Omega_m = 0.27$ , and  $\Omega_\Lambda = 0.73$  (Komatsu et al. 2009), which corresponds to a luminosity distance  $D_L = 6141.3 \text{ Mpc}$ , an angular size distance  $D_A = 1631.8 \text{ Mpc}$ , and a linear scale of  $7.91 \text{ pc mas}^{-1}$  at the source redshift. We use positively-defined spectral index  $\alpha = d \ln S / d \ln \nu$ .

## 2 OBSERVATIONAL DATA

Blazar 0235+164 was observed on 2 September 2008 with the Very Long Baseline Array<sup>2</sup> (VLBA; Napier 1994), a network of ten identical 25-m antennas spread across the US providing baselines of up to 8600 km. The VLBA's frequency agility was used to perform imaging simultaneously at seven frequencies (4.6/5.0, 8.1/8.4, 15.4, 23.8, and 43.2 GHz). Eight 8 MHz-wide frequency channels (IFs) were recorded at 128 Mbps with 1-bit sampling. The 5 and 8 GHz data were split into two sub-bands (four IFs each) to provide independent measurements at close frequencies. The observation included 13 on-source scans (each 3-7 minutes long depending on frequency) spread over 8 hours. The data were correlated at the Array operation center in Socorro. This observation was conducted in the framework of our survey of parsec-scale radio spectra of twenty  $\gamma$ -ray bright blazars (Sokolovsky et al. 2010a,b).

Another observations set was performed by the European VLBI Network at bands S/X (2.3 and 8.4 GHz) on 19 October 2008, C (5 GHz) on 22 October 2008 and L (1.7 GHz) on 29 October 2008. Each band included 8 IFs of 8 MHz width. C and L bands were recorded in right and left circular polarizations, while S and X bands – in the right one with the full bitrate 512 Mbit/s. Correlation was performed at Joint Institute for VLBI<sup>3</sup>.

The a priori amplitude calibration, phase calibration with the phase-cal signal injected during observations, fringe fitting (performed separately for each IF) and bandpass correction were applied in AIPS (Greisen 1990). The hybrid imaging (Walker 1995) including iterations of image deconvolution using the CLEAN algorithm (Högbom 1974) followed by amplitude and phase self-calibration were performed in Difmap (Shepherd 1997). We applied a special procedure involving preliminary imaging used to determine residual antenna gain corrections that are persistent in time and appear for all the observed sources (a similar procedure was utilized by Sokolovsky et al. 2011). The resulting amplitude calibration accuracy is expected to be  $\sim 5\%$  in the 4.6–15.4 GHz range and  $\sim 10\%$  at 23.8 and 43.2 GHz. Details of the employed calibration and analysis technique are described by Sokolovsky (2011).

The clean maps of 0235+164 on different frequencies are shown in Figure 1. Both multi-frequency experiments fall on the prominent radio flare in the source.

<sup>1</sup> [http://astrogeo.org/vlbi/solutions/rfc\\_2016c/](http://astrogeo.org/vlbi/solutions/rfc_2016c/)

<sup>2</sup> <https://science.nrao.edu/facilities/vlba>

<sup>3</sup> <http://www.jive.nl/>

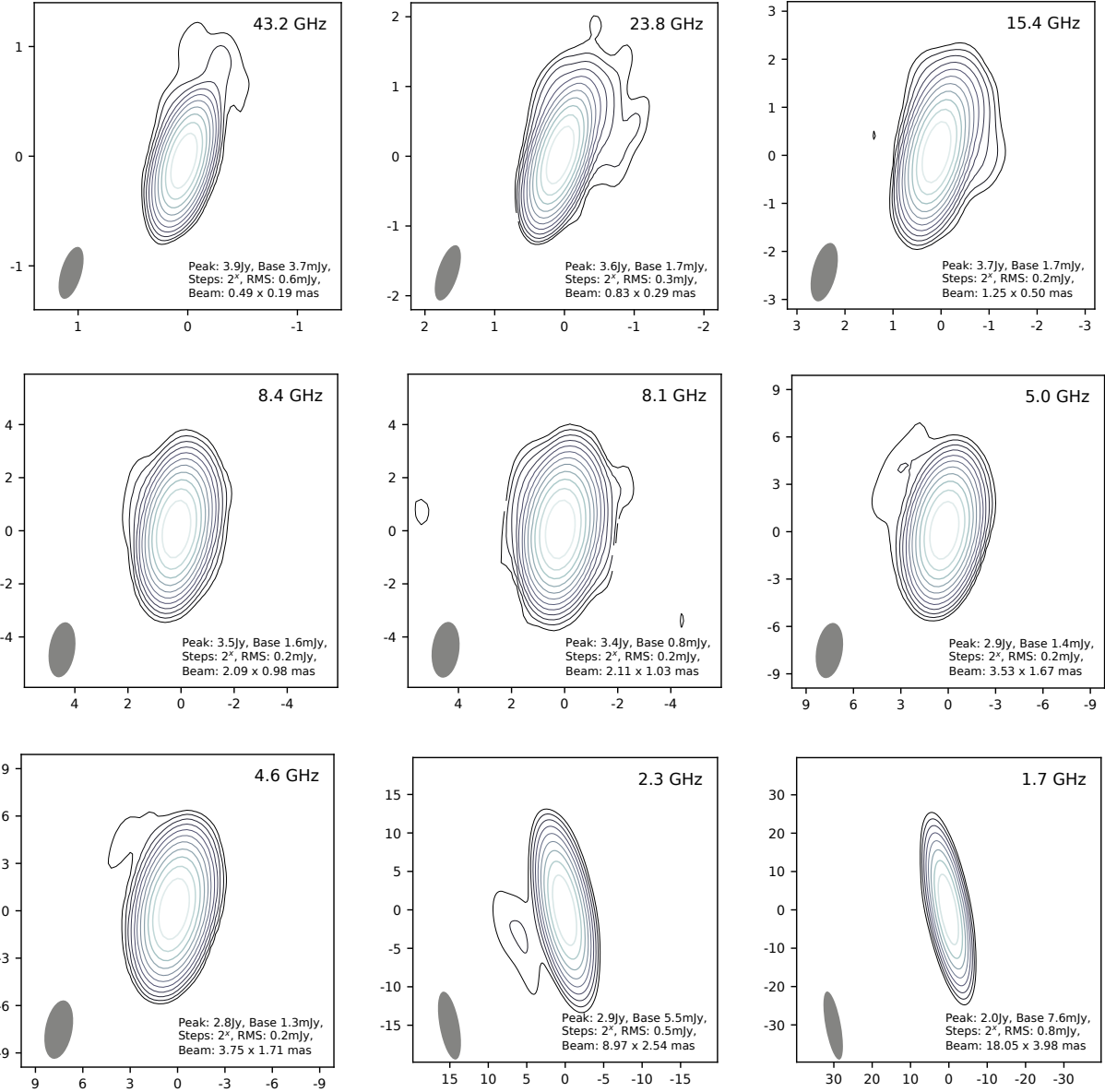


**Figure 1.** 0235+164 clean maps in RA-Dec axes. The beam size (at half maximum) is plotted in the lower left corner.

We also use 100 VLBA observations at 43 GHz by Boston University blazar group<sup>4</sup> covering 2007–2016.

The single-dish flux density monitoring observations (Figure 2) of 0235+164 were obtained with the 26-m radio telescope of University of Michigan Radio Observatory<sup>5</sup> (UMRAO) at 4.8, 8.0 and 14.5 GHz, 40-m telescope of Owens Valley Radio Observatory<sup>6</sup> (OVRO) at 15 GHz (Richards et al. 2011), and 14-m telescope of Metsähovi Radio Observatory<sup>7</sup> telescope at 22 and 37 GHz. Data by OVRO and UMRAO at 15 GHz are combined together.

Blazar 0235+164 is a target of RadioAstron AGN survey (Kovalev et al., in prep). It is monitored regularly at L (1.6 GHz), C (4.8 GHz) and K (22.2 GHz) bands by the spacecraft antenna along with ground-based telescopes in interferometric mode. Typical observations set lasts for 40–60 minutes and is performed either in single band with two circular polarizations or dual band with one circular polarization each. Correlation is performed at Astro Space Center using software correlator (Kardashev et al. 2013, Likhachev et al. 2017). Post correlation handling (fringe fitting, calibrations) is performed using PIMA<sup>8</sup> software (Petrov et al. 2011). We analyze 12 observations epochs from Dec 2012 till Jan 2016, summarized in Table 3.

<sup>4</sup> [http://www.bu.edu/blazars/VLBA\\_GLAST/0235.html](http://www.bu.edu/blazars/VLBA_GLAST/0235.html)

<sup>5</sup> <http://lsa.umich.edu/astro>

<sup>6</sup> <http://www.astro.caltech.edu/ovroblazars/>

<sup>7</sup> <http://metsahovi.aalto.fi/en/>

<sup>8</sup> <http://astrokeo.org/pima>

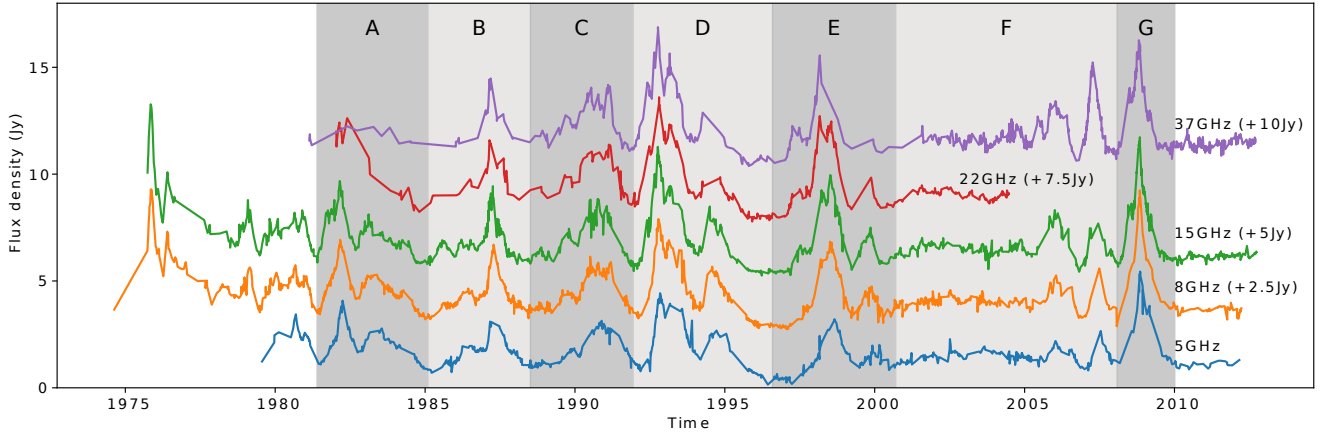


**Figure 2.** The light curves of AO 0235+164 at 4.8 – 37 GHz (shifted along y-axis for better visualization). Shaded areas denote the epochs of interest (see text for details).

### 3 VLBI ANALYSIS

We model the VLBI structure of 0235+164 at each frequency with elliptical Gaussian core and circular Gaussian component(s) in the  $uv$ -plane using `Difmap`. We choose elliptical core based on comparison of this model with point source and circular Gaussian models using the  $K$ -fold cross-validation criteria (Hastie et al. 2009). In this approach the baselines are divided randomly into  $K$  sets, then models are refitted to  $K-1$  sets and their prediction on the  $K$ -th set are compared. We also vary  $K \in [3, 10]$  for sake of robustness. Elliptical model is found to better describe the data. The extended structure, if any, is weak and does not affect core parameters significantly. The errors of the models parameters are estimated in the image plane following Fomalont (1999).

Additionally we compare the size of the fitted core with the resolution limit proposed by Kovalev et al. (2005) for gaussian brightness distribution template. The core is resolved at all frequencies except for 1.7 GHz and almost at all epochs of the 7 mm long-term monitoring data. If the core is unresolved, we use the corresponding resolution limit for its major and minor axes size. Models for the multi-frequency experiments are summarized in Table 1.

We use the same approach to model the 7 mm VLBA monitoring data. In several cases we also use CLEAN-components to better describe the extended emission, which is applicable since the core is prominent enough and isolated at most epochs/frequencies. Evolution and frequency dependence of the core parameters is discussed further.

### 4 LIGHT CURVES ANALYSIS

The variability time delays between light curves can be found using several methods based ether on data modeling or cross-correlation techniques. The former imply some prior knowledge about the data (e.g. Gaussian shapes of the flares (Pyatunina et al. (2007), Kudryavtseva et al. (2011) or two-sided exponential profiles (Valtaoja et al. (1999), Hovatta et al. (2009)). Moreover, one have to divide the light

**Table 1.** Source models for the two multi-frequency experiments. Columns: (1) – frequency, (2) – component ID, (3–8) – standard `Difmap` format: Flux, Radius, Position angle, Major axis, Axial ratio, Major axis orientation angle.

Freq. (GHz)	ID (1)	$S$ (Jy) (3)	$R$ (mas) (4)	$\theta_c$ (deg) (5)	$b_{maj}$ (mas) (6)	$e$  (7)	$\Phi$ (deg) (8)
43.2	C0	3.498	0.027	171	0.058	0.56	7.7
	C1	0.636	0.146	-178	0.064		
	C2	0.051	0.149	113	< 0.001		
	C3	0.062	0.613	-18	0.837		
23.8	C0	3.714	0.015	2	0.115	0.43	24.0
	C1	0.046	0.204	88	0.174		
	C2	0.110	0.634	-22	0.714		
	C3	0.163	0.725	-18	0.821		
8.43	C0	3.378	0.038	-28	0.197	0.56	-13.6
	C1	0.258	0.686	-23	0.802		
8.11	C0	3.288	0.035	-51	0.196	0.45	-26.3
	C1	0.247	0.729	-23	0.772		
	C2	0.163	0.725	-18	0.821		
5.0	C0	2.758	0.057	-42	0.328	0.57	-10.9
	C1	0.288	0.669	-22	1.127		
4.61	C0	2.642	0.097	-39	0.346	0.51	-16.8
	C1	0.297	0.678	-22	1.189		
	C2	0.163	0.725	-18	0.821		
8.39	C0	6.457	0.049	-173	0.197	0.56	5.0
	C1	0.374	0.447	-21	0.655		
	C2	0.015	1.550	79	1.001		
4.97	C0	4.897	0.032	143	0.290	0.46	0.7
	C1	0.414	0.588	-16	1.003		
	C2	0.163	0.725	-18	0.821		
2.27	C0	2.987	0.057	-163	0.772	0.73	-11.0
	C1	0.015	2.864	-48	< 0.001		
	C2	0.037	6.164	112	5.684		
1.66	C0	2.069	0.093	19	< 1.590	0.60	2.1
	C1	0.010	4.315	61	< 0.001		
	C2	0.010	4.902	-24	0.009		

curve into separate flares manually, which is the subject of human factor bias. The latter methods are based on calculation of mutual cross-correlation function (CCF) of the light curves and do not involve additional information about their structure (e.g. standard correlation function with interpolation (ICCF) or discrete correlation function (DCF; [Edelson & Krolik \(1988\)](#)). However these methods require sufficient amount of data to perform well and also imply some parameters which may affect the results, like size of the bin used for interpolation or for DCF evaluation (see [White & Peterson \(1994\)](#) for ICCF/DCF comparison and references).

Another approach, which also does not require any prior knowledge about the data is Gaussian process regression (GPR; [Rasmussen & Williams 2005](#)) – a special case of Bayesian non-parametric models. GPR is actively used in many fields of science including astronomy. It has been recently applied to the light curves of blazar PKS 1502+106 by [Karamanavis et al. \(2016\)](#).

GPR is a prior probability distribution over functions. It is characterized by its mean value and covariance matrix. The former can be set to zero by shifting the data, the latter is expressed through covariance function (*kernel*). The kernel depends on *hyperparameters*, which are determined for given data by maximizing marginal likelihood function (*training* the GP).

The mostly often used kernel for time series is squared exponential (SE):

$$C_{SE}(x_i, x_j) = A^2 \exp\left(\frac{-(x_i - x_j)^2}{2l^2}\right), \quad (1)$$

where  $l$  is characteristic scale indicating the connection between  $x_i$  and  $x_j$ , and  $A$  reflects the distribution of function values around the mean.

In case of longer light curves containing several or multi-peaked flares the single SE kernel 1 might not perform well due to presence of more than one characteristic scales in the source variability. This is the case for blazars, which are known to vary on a range of timescales and usually possess “red” power spectra. To overcome this one may use a sum of several SE-kernels. An infinite weighted sum may be represented by the rational quadratic (RQ) kernel ([Rasmussen & Williams 2005](#), Chapter 4):

$$C_{RQ}(x_i, x_j) = A^2 \left(1 + \frac{(x_i - x_j)^2}{(2\varepsilon l^2)}\right)^{-\varepsilon} \quad (2)$$

The relative weighting of different time scales variations is specified by hyper parameter  $\varepsilon \in (0, +\infty)$ . In the limit of  $\varepsilon \rightarrow +\infty$  the RQ kernel becomes an SE kernel.

We use the kernel represented by a sum of RQ-kernel and a white noise one:

$$C(x_i, x_j) = C_{RQ}(x_i, x_j) + (x_i - x_j)\sigma_n^2 \quad (3)$$

with the hyperparameters  $A, l, \alpha$  of RQ-kernel and  $\sigma_n$ , which characterizes random noise of the observed data.

We also take into account the uncertainties of estimated hyperparameters by integrating the distributions along corresponding axes ([MacKay 2003](#)).

In order to check whether there is a difference between time lags on different epochs we split our data into seven

time intervals each having at least one flare and containing more or less sufficient data for analysis. The selected intervals are denoted in Figure 2.

GPR is performed using `george` python library ([Ambikasaran et al. 2014](#)). For sampling the posterior distributions of hyperparameters we employ `emcee` Markov chain Monte Carlo (MCMC) sampler ([Foreman-Mackey et al. 2013](#)).

From the obtained posterior distributions we estimate time and flux density of each flare peak. These results are summarized in Table 2. Separate flares and the corresponding time delays are shown in Figure 4.

As an example, the results of implementing GPR to the 15 GHz light curve of epochs interval 1985 – 1988 (labeled B) are shown in Figure 3. Histograms illustrate the obtained posterior distributions of hyperparameters (the plot is produced with `corner` package by [Foreman-Mackey 2016](#)). Median and 16/84 percentiles are shown by vertical lines. In the upper right corner the light curve is shown along with  $\pm 3\sigma$  (99.7%) confidence interval for GPR. Note the outlier data point near the flare peak which is effectively bypassed by GPR, but certainly would be a challenge for cross-correlation methods. As expected, the confidence interval widens within data gaps.

We also apply DCF method to the time intervals labeled in Figure 2. In order to estimate the errors of the obtained delays we perform Monte Carlo simulations and modified bootstrapping or flux randomization / random subsample selection (FR/RSS) method proposed by [Peterson et al. 1998](#)). This allows one to account for errors due to initial flux measurements uncertainties as well as for possible outliers in the data. To account for the possible influence of the selected time bin we vary it in each simulation to be uniformly spread in the range  $[\Delta t_{mean} - \Delta t_{mean}/2, \Delta t_{mean} + \Delta t_{mean}/2]$  (where  $\Delta t_{mean}$  is the mean time span between the observations). The obtained results are similar to GPR but have huge uncertainties, which makes their further analysis impracticable. The following discussion is based on the results obtained with the GPR method.

## 5 TIME LAGS VS. FREQUENCY

We approximate dependence of the time lags  $\Delta T$  on frequency  $\nu$  (comparative to the peak at highest one) with model  $\Delta T = a_t \nu^{-k_t} + b_t$ . `Emcee` MCMC sampler is used with uniform prior distributions for  $a_t$  and  $b_t$  and normal prior distribution for index  $k_t = 0.90 \pm 0.44$  ([Pushkarev & Kovalev 2015](#)). We assume here that the observed time lags between flares peaks at different frequencies are caused by the same intrinsic opacity mechanism, which is responsible for the core shift (and changing of the core size) effect, i.e. synchrotron self-absorption. This assumption is used to set the aforementioned prior distribution for the sought parameter  $k_t$ . Parameter  $b_t < 0$  corresponds to the delay between flare at a given highest frequency and “infinite” frequency,  $a_t > 0$  characterizes jet velocity, and  $k_t$  reflects the opacity mechanism and geometry of the jet. It also can be connected with the distributions of magnetic field strength and particle density along the jet.

As seen in Figure 4 the obtained peak-to-peak delays differ from one flare to another. Moreover, there are flares

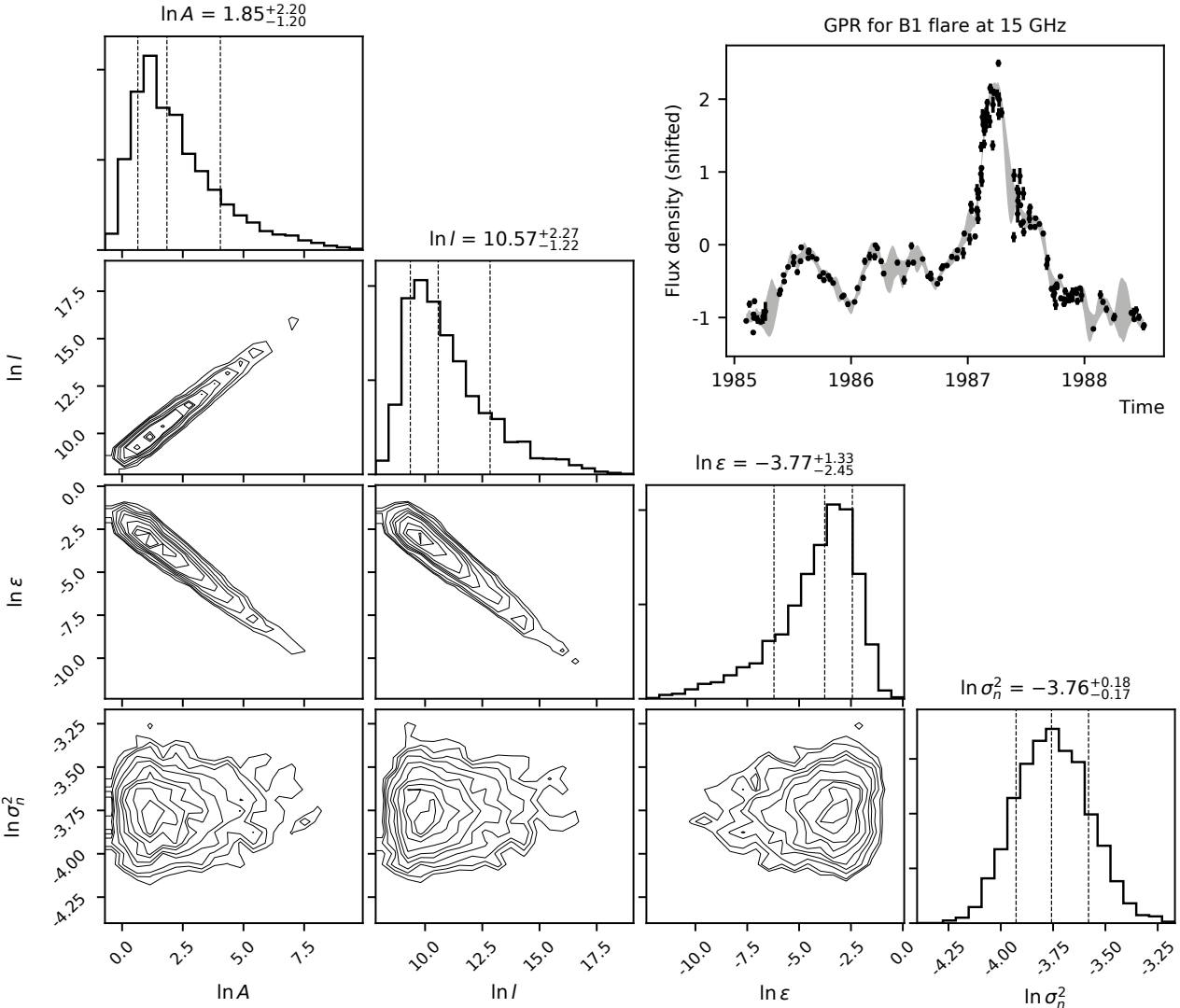


**Figure 3.** Application of GPR to 15 GHz B-flare: the posterior distributions of GP hyperparameters (dashed lines indicate 16, 50 and 84 percentiles). The light curve with mean flux density subtracted is shown in the upper right corner, shaded area denotes  $\pm 3\sigma$  confidence interval of GPR.

with unusual lags when a peak comes earlier on lower frequency. (Table 2).

Similar unexpected time delays in the source have been reported by Kraus et al. (1999) for short flare in 1992 which is a part of D-flare in our notation.

We obtain a wide range of parameter  $k_t \in [0.7; 1.8]$  with median value  $k_t = 1.2$ . The posterior  $k_t$  distributions are plotted on Figure 5 for the two marginal cases (D1-flare with  $k_t = 1.8$  and F2-flare with  $k_t = 0.7$ ), showing the difference between obtained  $k_t$  with confidence more than 95%.

We find no correlation between  $k_t$  and peak flux density for the flares, neither somewhat monotonic changing of  $k_t$  in time.

Different values of index  $k_t$  within one source for separate flares have been also reported by Kudryavtseva et al. (2011). The reason for its changing is not obvious, and may be related either to measurements uncertainties due to lack

of data or intrinsic changes in the jet, e.g. when the injected particles distort the profile of initial electron distribution of a steady outflow.

On the last panel of Figure 4 the light curves of 37 GHz single dish, 43 GHz core and 43 GHz superluminal component  $G_c$  are shown (see also § 8.2). Peak-to-peak time delay between the component and the core flares obtained using GPR is  $T_{G_c,max} - T_{Core,max} = 21 \pm 4$  days. One can see, that the total flux measured by single-dish telescope is a sum of the core and  $G_c$  and has maximum somewhere in the middle between their peaks. Obviously, this yields to incorrect interpretation of the single-dish flare peak as a passage time of a disturbance through the core, and may be responsible for the different values of  $k_t$ .

Another noticeable effect is that the single dish flare profile is much smoother than one of the core. But the former is often treated as the latter and used for brightness temperature and Doppler factor estimates. In this case there

**Table 2.** GPR results: peak time ( $T_m$ , MJD) and flux density ( $F_m$ , Jy) of the flares at 37 – 5 GHz. Values are median, 84/16 percentiles (and median absolute deviation in brackets).

		37 GHz	22 GHz	15 GHz	8 GHz	4.8 GHz
A1	$T_m$	...	...	$45030^{+2}_{-1}(1.4)$	$45034^{+2}_{-2}(1.8)$	$45057^{+6}_{-5}(5.9)$
	$F_m$	...	...	$4.53^{+0.04}_{-0.04}$	$4.30^{+0.02}_{-0.03}$	$3.65^{+0.07}_{-0.06}$
B1	$T_m$	$46866^{+14}_{-9}(10.3)$	$46857^{+5}_{-17}(8.8)$	$46888^{+8}_{-3}(5.5)$	$46900^{+3}_{-3}(2.9)$	$46913^{+15}_{-8}(11.9)$
	$F_m$	$4.49^{+0.22}_{-0.14}$	$4.15^{+0.21}_{-0.13}$	$4.09^{+0.03}_{-0.04}$	$4.01^{+0.05}_{-0.05}$	$3.32^{+0.19}_{-0.21}$
D1	$T_m$	$48904^{+4}_{-3}(3.4)$	$48912^{+5}_{-4}(5.1)$	$48903^{+1}_{-1}(0.9)$	$48911^{+1}_{-1}(1.1)$	$48930^{+1}_{-4}(2.2)$
	$F_m$	$6.70^{+0.13}_{-0.11}$	$5.84^{+0.10}_{-0.09}$	$6.11^{+0.04}_{-0.05}$	$5.31^{+0.04}_{-0.04}$	$4.17^{+0.02}_{-0.02}$
E1	$T_m$	$50873^{+3}_{-3}(2.8)$	$50876^{+3}_{-2}(2.4)$	$50907^{+10}_{-8}(9.1)$	...	...
	$F_m$	$5.30^{+0.13}_{-0.10}$	$5.08^{+0.07}_{-0.07}$	$4.01^{+0.07}_{-0.07}$	...	...
E2	$T_m$	...	$51001^{+5}_{-8}(6.6)$	$51015^{+4}_{-3}(3.8)$	$51008^{+2}_{-2}(2.1)$	$51027^{+7}_{-10}(8.0)$
	$F_m$	...	$4.80^{+0.14}_{-0.14}$	$4.56^{+0.15}_{-0.15}$	$4.18^{+0.04}_{-0.05}$	$3.25^{+0.03}_{-0.05}$
E3	$T_m$	...	...	$51492^{+1}_{-2}(1.6)$	$51496^{+7}_{-5}(6.2)$	$51530^{+3}_{-4}(3.7)$
	$F_m$	...	...	$2.30^{+0.02}_{-0.02}$	$2.02^{+0.05}_{-0.04}$	$1.66^{+0.02}_{-0.01}$
F1	$T_m$	$53723^{+9}_{-13}(11.7)$	...	$53752^{+7}_{-6}(6.3)$	$53763^{+5}_{-4}(4.6)$	$53752^{+1}_{-2}(1.5)$
	$F_m$	$3.42^{+0.12}_{-0.13}$	...	$3.26^{+0.04}_{-0.04}$	$2.62^{+0.04}_{-0.04}$	$2.06^{+0.02}_{-0.01}$
F2	$T_m$	$54203^{+4}_{-4}(3.7)$	...	$54251^{+14}_{-12}(13.1)$	$54269^{+6}_{-8}(7.3)$	$54290^{+7}_{-6}(6.8)$
	$F_m$	$4.96^{+0.11}_{-0.11}$	...	$2.78^{+0.14}_{-0.09}$	$3.09^{+0.08}_{-0.07}$	$2.39^{+0.09}_{-0.09}$
G1	$T_m$	$54764^{+3}_{-2}(2.7)$	...	$54770^{+1}_{-0}(1)$	$54774^{+1}_{-2}(1.2)$	$54784^{+2}_{-1}(1.9)$
	$F_m$	$6.00^{+0.12}_{-0.13}$	...	$6.48^{+0.03}_{-0.03}$	$6.57^{+0.05}_{-0.05}$	$5.37^{+0.06}_{-0.07}$

must be a bias due to overestimation of the variability time scale. Indeed, the light curve of the core flare differs from a typical single-dish one, and, in contrast, has smoother raise and steeper decay. Therefore, the variability time scale may differ for different spatial resolution (see also section 7).

## 6 CORE SIZE AND SPECTRUM

Apparent size of a VLBI core depends on observations frequency. The photosphere interpretation assumes that this dependency follows the same power law as for the core shift (i.e.  $W_{core} \propto \nu^{k_w}$ , with  $k_w$  close to 1). This was shown for simultaneous multi-frequency observations by Kutkin et al. (2014) for blazar 3C 454.3 and achieved statistically for large ANG samples by Yang et al. (2008) ( $k_w = -0.95 \pm 0.37$ ) and by Pushkarev & Kovalev (2015) ( $k_w = -0.90 \pm 0.44$ ) for the sources located at Galaxy latitudes higher than  $\sim 10^\circ$ , while for Galactic plane residents the power index is closer to  $k_w \approx -2$  due to interstellar scattering.

The core in both VLBI experiments is modeled with

elliptical Gaussian with mean axial ratio  $\epsilon \sim 0.5$  (see Table 1). The dependence of its major and minor axes (FWHM of the Gaussian) on frequency is approximated with model  $W(\nu) = a_w \nu^{-k_w}$  (absence of an additional constant term here suggests that the core has “zero” size at “infinite” frequency). Since there is no significant difference between the core size obtained from two VLBI experiments at 5 and 8 GHz, we merge these data for better fit representation (see Figure 6).

Both major and minor axes follow the power law with  $k_{w,maj} = k_{w,min} = 0.8 \pm 0.1$  ( $a_{w,maj} = 1.1 \pm 0.1$ ,  $a_{w,min} = 0.65 \pm 0.07$ ), which is in good agreement with the photosphere scenario.

Since the modeled core size at L-band does not fulfill the resolution criteria, the upper limit is used. The core at S-band (2.3 GHz) is formally resolved, however, its size is still higher than expected from synchrotron self absorption model. To check whether there is an interstellar scattering coming into play on these frequencies we find the corresponding angular broadening for the given coordinates ( $\Theta_S = 0.16$  mas) from the NE2001 model (Cordes & Lazio

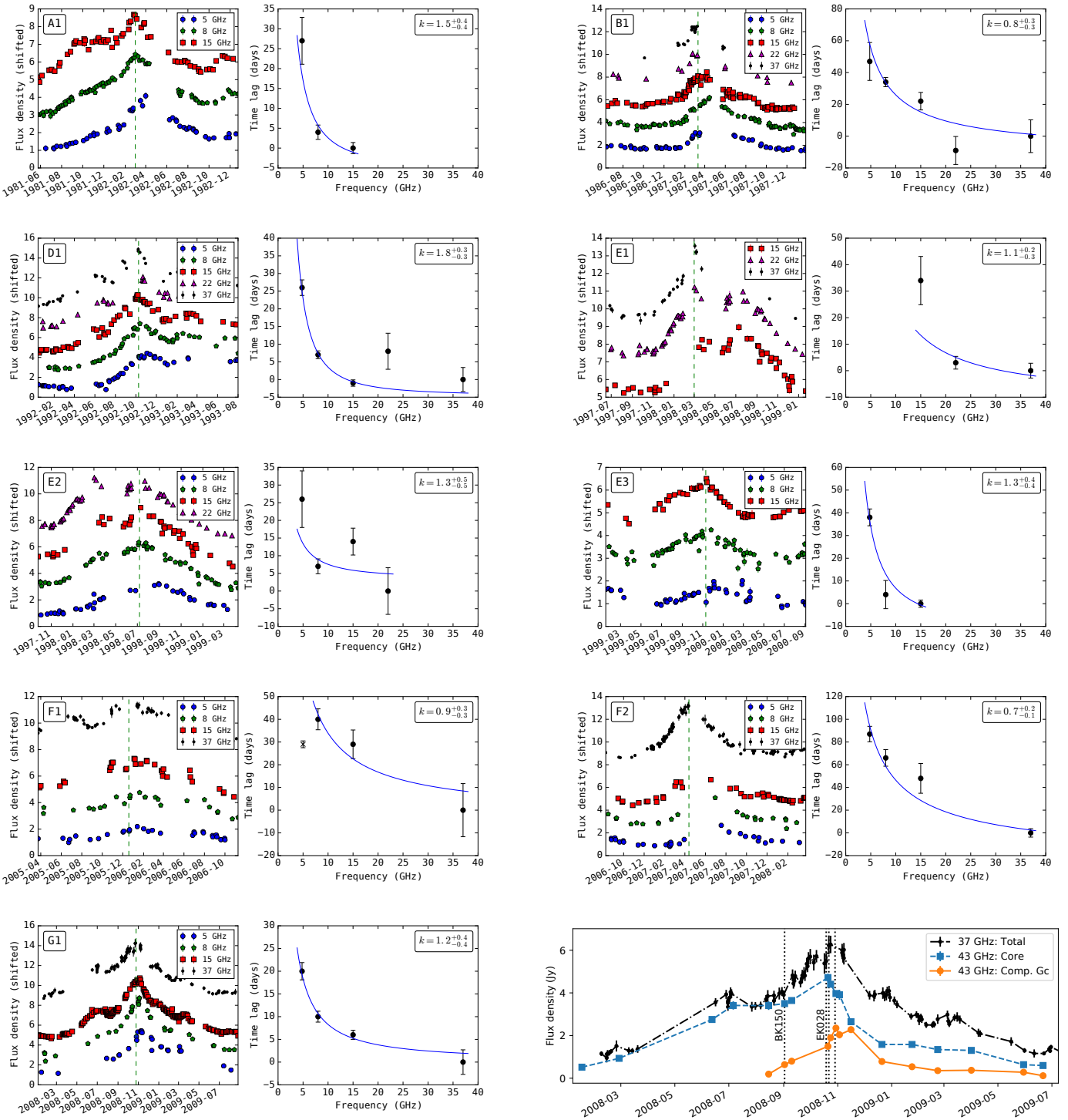


**Figure 4.** Plots of separate flares and the corresponding time lags. Vertical dashed lines mark the peak time at highest frequency. The last panel shows light curves of single-dish 37 GHz, the core, and the component Gc. Multi-frequency VLBI experiments marked with vertical dotted lines.

2002). This is significantly lower than the core size obtained from modeling, suggesting either that the scattering is not implicated here or there is really much denser Galactic medium at that direction. We also note, that excluding data at L and S bands doesn't affect results of the fit.

The power index found for the core size  $k_w$  coincides within the errors with one, obtained for the time lags, but is measured with much better accuracy. Therefore, the former can be used to constrain the latter and other model-fit parameters of the time lags dependence. For that purpose

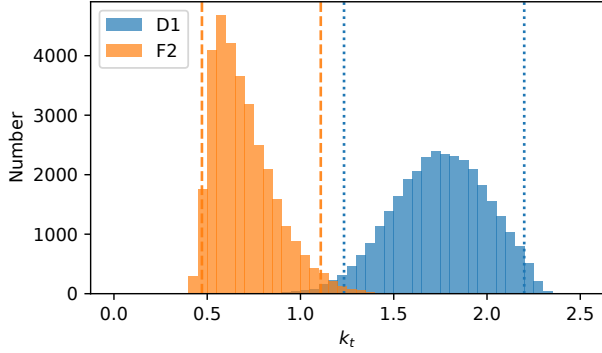


**Figure 5.** Posterior distributions of  $k_t$  parameter for D1 and F2 flares. Vertical dotted and dashed lines denote corresponding 95% intervals.

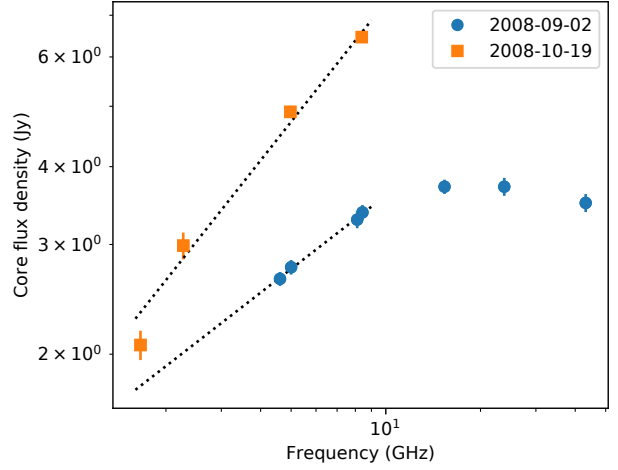


**Figure 7.** Core spectrum for two epochs during the flare.

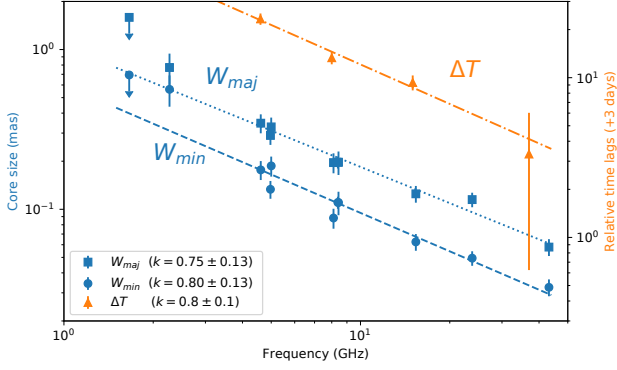


**Figure 6.** Core size  $W$  (left axis) and time lags of the G-flare peaks  $\Delta T$  (right axis) vs. observations frequency.

we employ the `emcee` sampler with narrow prior distribution for  $k_t = k_w = 0.8 \pm 0.1$  and obtain the resulting distributions of the other two parameters, yielding  $a_t = 80 \pm 14$ , and  $b_t = -3 \pm 2$  days.

Spectrum of the core is shown on Figure 7 for two multi-frequency experiments (the core flux density at a given band is assumed to remain constant during the experiment). The optically thick index increases from  $\alpha_1 = 0.39 \pm 0.09$  to  $\alpha_2 = 0.64 \pm 0.05$ , which might be related to the fact that peak at lower frequencies is lagged with respect to higher.

## 7 BRIGHTNESS TEMPERATURE AND DOPPLER FACTOR

Provided the models of visibility data, it is possible to estimate the apparent brightness temperature of a jet component in the source frame (Kovalev et al. 2005):

$$T_b = 1.22 \cdot 10^{12} \frac{S(1+z)}{\nu^2 W_{maj} W_{min}} (K), \quad (4)$$

where  $S$  – flux density in Jy,  $W_{maj}$  and  $W_{min}$  – major and minor apparent size in mas (FWHM of Gaussian model),  $z$  – redshift, and  $\nu$  – observing frequency in GHz.

On the other hand it is possible to estimate the so called variability brightness temperature in the source frame within the assumption that the variability time scale  $t_{var}$  corresponds to the light-crossing time of the component size (Hovatta et al. 2009):

$$T_{b,var} = 1.05 \cdot 10^8 \frac{D_\ell^2 S_{obs}}{(1+z)\nu^2 t_{var}^2} (K), \quad (5)$$

where  $D_\ell$  – luminosity distance in Mpc,  $S_{obs}$  – flux density in Jy,  $\nu$  – observations frequency in GHz,  $t_{var}$  – variability timescale in years.

$T_b$  and  $T_{var}$  are measured experimentally and can be expressed through an intrinsic brightness temperature, amplified by Doppler boosting (e.g. Kellermann et al. 2007):

$$\begin{cases} T_b = \delta T_{int} \\ T_{b,var} = \delta^3 T_{int}, \end{cases} \quad (6)$$

where  $\delta$  is Doppler factor. System solution gives  $\delta$  and  $T_{int}$ .

We adopt the following parameters:  $D_\ell = 6142$  Mpc,  $z = 0.94$ ,  $S_{obs} = 4.7$  Jy – peak value of the core flux density during G-flare, and  $t_{var} = 0.09$  yr – timescale of the core variability during G-flare. Note, that its profile has a plateau and differs from the two-sided exponential. Moreover, the flare decays faster than rises. We estimate the scale using time intervals and flux change various observations  $i, j$  during the flare as  $t_{var} = |(t_i - t_j)/\ln(S_i/S_j)|$  taken on the flare decay (epoch 2008-11-03).

We obtain  $T_{b,var} = 6.4 \cdot 10^{14}$  K and  $T_b = 1.5 \cdot 10^{12}$  K, which yields to  $\delta \approx 21$ , and  $T_{int} \approx 7 \cdot 10^{10}$  K. This value is close to the equipartition brightness temperature  $T_{eq} \simeq 5 \cdot 10^{10}$  K, suggested by Readhead (1994).

In Figure 8 the core flux is shown along with derived  $T_b$ . Note that during the flares (2008 and 2015) brightness temperature increases by a factor  $\sim 2$ .

Here we use self consistent system to estimate Doppler

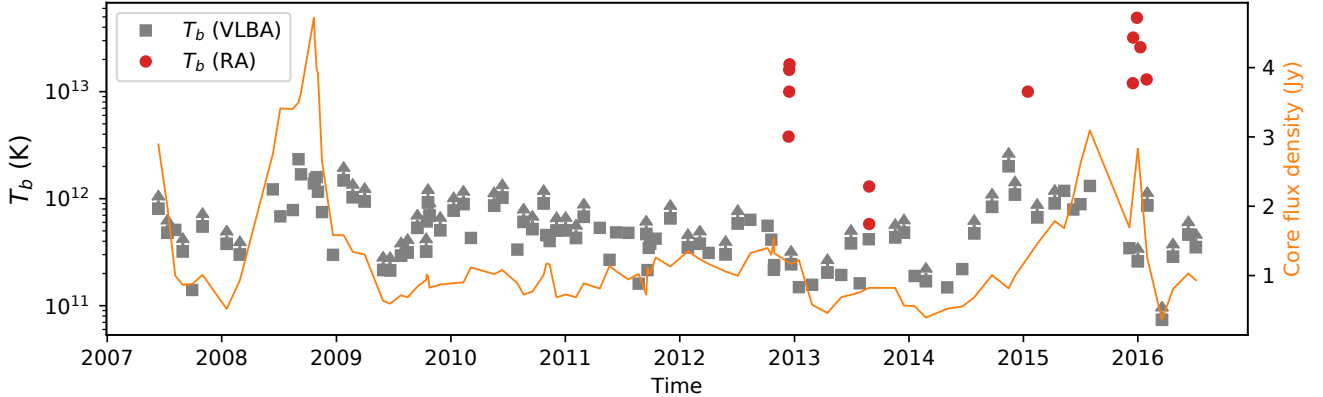


**Figure 8.** Brightness temperature by 7 mm VLBA (squares) and RadioAstron (circles). Arrows mark  $T_b$  estimated using corresponding resolution limits. The curve shows core flux density (right axis).

factor and intrinsic brightness temperature, considering the size and variability timescale of the same region.

### 7.1 Brightness temperatures by RadioAstron

Assuming that the brightness distribution has Gaussian profile we estimate the lower limit of  $T_b$  following Lobanov (2015):

$$T_{b,min} = \frac{\pi e}{2k_B} B^2 V_B \approx 3.09 \left( \frac{B}{km} \right) \left( \frac{V_B}{mJy} \right) [K], \quad (7)$$

where  $k_B$  is Boltzmann constant,  $B$  – baseline projection,  $V_B$  – visibility amplitude, measured on that baseline.

We also estimate  $T_b$  using the size inferred from modeling the visibility amplitudes on ground-ground and ground-space bases with circular Gaussian profile.  $T_b$  and size estimates are shown in columns (5-6) in Table 3. The estimates of  $T_b$  are plotted in Figure 8 with circles.

The highest brightness temperature estimate comes from fringe detection on 26 Earth diameters in C-band. The longest baseline in wavelengths is 14 G $\lambda$  achieved at K-band. Note, that at these bands the interstellar scattering does not seem to play significant role in the observed source structure (Johnson et al. 2016). Therefore, brightness temperature measured by RadioAstron is about an order of magnitude higher than one obtained from VLBA observations (Figure 8). Ground-space interferometer begins resolving compact sub-structure of the source, which could not be inferred from ground-only observations.

Among possible reasons and explanations of ultra-high apparent brightness temperatures are the following: i) the real jet speed is much higher than one, derived from kinematics of components; ii) continuous injection or re-acceleration of relativistic electrons that compensates the inverse Compton losses; iii) synchrotron emission of relativistic protons; iv) exotic models like mono-energetic spectrum of particles, etc. However, all these models come into collision with observational facts. See also discussion by Kovalev et al. (2016), who reported similar extreme brightness temperatures in blazar 3C 273.

**Table 3.** RadioAstron observations of 0235+164. Columns are: (1) Date, (2) Band, (3) Projected baseline (in Earth diameters), (4) Lower limit of brightness temperature, (5) Estimate of brightness temperature, (6) Estimate of circular Gaussian component size.

Date (1)	Band (2)	$D/D_\oplus$ (3)	$T_b^{min}$ (K) (4)	$T_b^{est}$ (K) (5)	$W$ ( $\mu$ as) (6)
2012-12-13	C	7.7	$2.0 \cdot 10^{12}$	$3.8 \cdot 10^{12}$	111.2
2012-12-15	C	14.9	$2.2 \cdot 10^{12}$	$1.0 \cdot 10^{13}$	70.3
2012-12-15	K	14.8	$9.2 \cdot 10^{12}$	$1.6 \cdot 10^{13}$	14
2012-12-16	C	18.7	$4.5 \cdot 10^{12}$	$1.8 \cdot 10^{13}$	54.4
2013-08-27	C	2.2	$3.9 \cdot 10^{11}$	$5.8 \cdot 10^{11}$	366.5
2013-08-27	L	2.8	$1.2 \cdot 10^{12}$	$1.3 \cdot 10^{12}$	470.6
2015-01-15	L	19.8	$1.5 \cdot 10^{12}$	$1.0 \cdot 10^{13}$	163.8
2015-12-16	C	8.7	$7.4 \cdot 10^{12}$	$1.2 \cdot 10^{13}$	92.9
2015-12-17	C	16.4	$7.8 \cdot 10^{12}$	$3.2 \cdot 10^{13}$	62.5
2015-12-29	C	25.5	$7.9 \cdot 10^{12}$	$4.9 \cdot 10^{13}$	43.0
2016-01-09	C	14.5	$1.2 \cdot 10^{13}$	$2.6 \cdot 10^{13}$	61.3
2016-01-29	C	8.9	$4.1 \cdot 10^{12}$	$1.3 \cdot 10^{13}$	108.2

An evidence for the former scenario comes from comparison of the core shift and time delays (Section 9). The apparent speed of the flow is an order of magnitude higher than the pattern speed estimated from kinematics of the superluminal component, implying an order higher Lorentz and Doppler factors. Note, that the intrinsic opening angle is close to the viewing angle, so there are parts of the jet viewed at zero inclination, which also increases Doppler factor. Regions with  $\delta \sim 200$  can produce the high apparent brightness temperatures. The corresponding angular scale of these regions is tens  $\mu$ as (see the last column in Table 3), so they can be resolved only by ground-space interferometer. The corresponding variability timescales there would be ten times shorter, about 0.01 yr. The several days variability

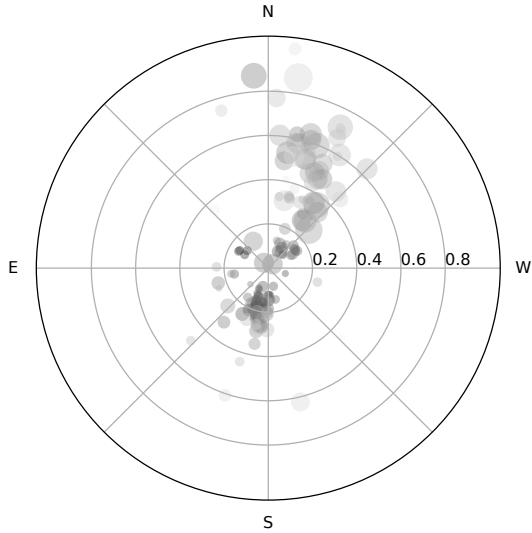


**Figure 9.** The model components within 1 mas of the core, aligned relative the position of the core (not plotted). The circles size and color intensity are proportional to the size and flux density of the components.

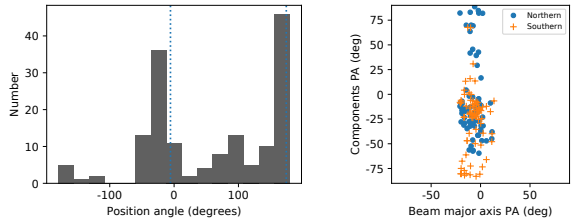


**Figure 10.** Distribution of the components position angles. Vertical lines show the median of beam major axis orientation. On the right panel position angle of the components (reduced to  $[-90^\circ, 90^\circ]$ ) vs. the position angle of the beam major axis.

is exactly what is observed in 0235+164 at radio and optical bands. Moreover, this variability has, probably, intrinsic nature (Qian et al. 2000, Romero et al. 2000).

## 8 JET STRUCTURE

### 8.1 Image stack

Due to extreme compactness of the source and weakness of its extended structure it is not possible to determine jet geometrical characteristics from a single VLBI observation. Moreover, even the direction of the jet is not clear. In Figure 9 all modeled components from 100 VLBA datasets are plotted with respect to the core position (the core is not shown). It is clearly seen that the components tend to concentrate almost symmetrically at two directions. We check if the position angles of the components (median  $-28^\circ$  and  $162^\circ$ ) correlate with the major axis of the beam (median  $-6^\circ$ ). They are found to be close but not coincide, neither showing correlation (Figure 10). So the beam does not seem

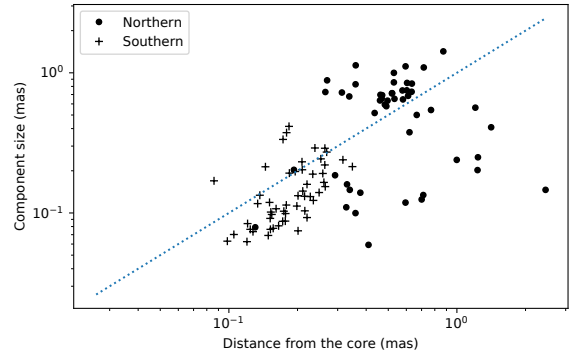


**Figure 11.** Size of the components vs. their distance from the core. The dotted line represents equality.

to be responsible for the observed phenomena. Another support comes from the fact that size of the components increases with distance from the core both in southern and northern directions. Moreover, in the northern part there are farther and larger components (see Figure 11). We interpret this as a bend of the outflow from south to north, so that the younger (closer to the central engine) jet is observed southwards and the older (more extended and prominent) is seen northwards of the core.

We combine 100 VLBA snapshots aligned by the core position into a stack image to increase dynamic range. This allows us to see the jet and construct the ridge line up to  $\sim 0.8$  mas north-northwest of the core as shown in Figure 12 (the southern ridge line would be too short to perform any calculations). The intensity along transverse jet slices measured down the ridge line is modeled with Gaussian profile, whose width being deconvolved with the beam represents the real jet width  $w$ . Apparent opening angle  $\varphi$  is then estimated as  $\varphi = 2 \arctan(w/2l)$ , where  $l$  is distance along the ridge line. The jet profile ( $w/2$  vs.  $l$ ) is shown in Figure 13. Assuming conical geometry we find  $\varphi_{43} = 60^\circ \pm 5^\circ$ . It is two times higher than the value obtained by Pushkarev et al. (2017) for stacked image at 15 GHz on larger scales ( $\varphi_{15} = 30^\circ$  on about 2 mas), suggesting that the jet is collimated somewhere within  $\sim 1.5$  mas of the core. On lower frequency (1.4 GHz, tens mas) the VLBA stacked image shows that jet changes its direction to north-northeast (Pushkarev et al. 2017) keeping the same opening angle  $\sim 30^\circ$ .

### 8.2 Gc component

G-flare is accompanied by a bright feature (Gc hereafter) located to the south-southeast from the core and traveling with superluminal apparent speed. It has been also studied by Agudo et al. (2011), who interpreted it as a moving transverse shock.

In Figure 16 the trajectory of Gc is shown relative to the core position, where seen its non-ballistic motion. The mean proper motion of Gc relative to the core is  $\mu = 0.20 \pm 0.03$  mas/yr, which corresponds to apparent speed  $\beta_{app} = 10 \pm 1.6 c$ . The position and speed of Gc is consistent with its ejection in Jan 2008, at the beginning of the core (and total flux) flare.

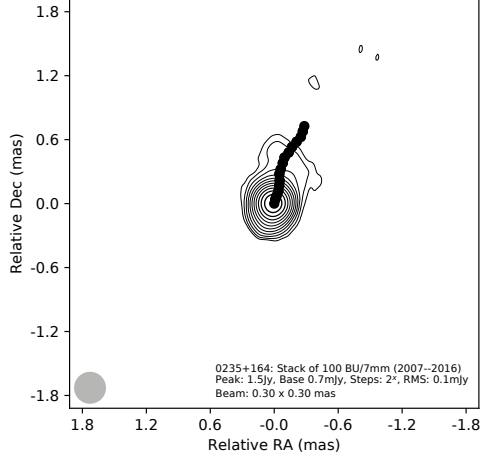


**Figure 12.** The stacked map of 0235+164 at 7mm. Black circles show the ridge line. Grey circle in the lower left corner shows the beam.

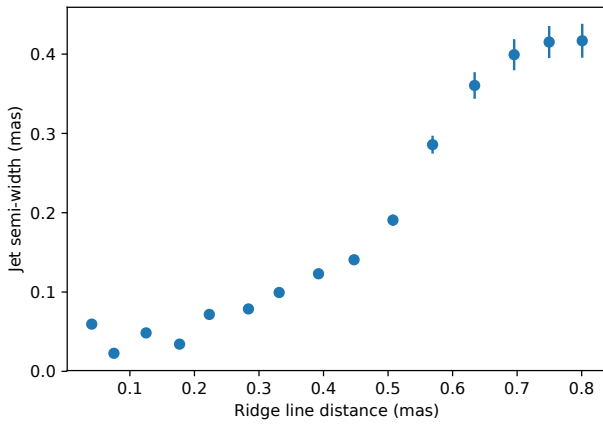


**Figure 13.** Jet half-width vs distance along the ridge line. Linear fit is shown with dotted line.

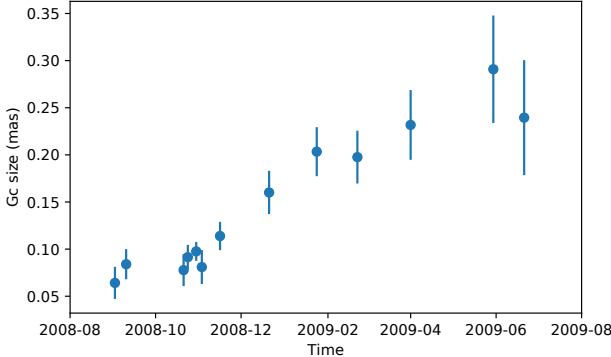


**Figure 14.** Size of Gc vs time.

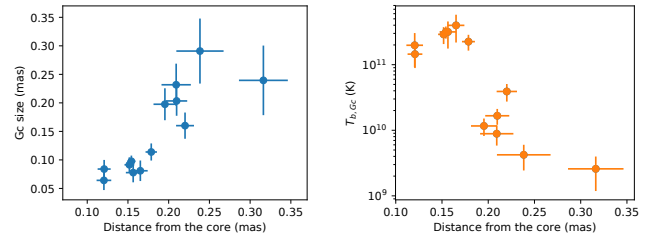


**Figure 15.** Size and apparent brightness temperature of Gc vs. its separation from the core.

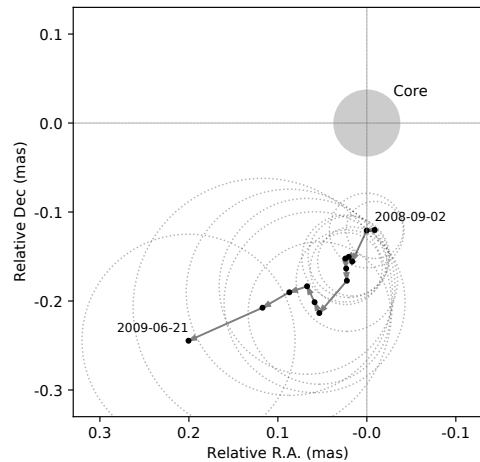


**Figure 16.** Trajectory of the Gc component during Sep 2008 – Jun 2009 at 43 GHz. Dots arrows and open circles show the position, path and size of the Gc. The core is at (0,0) and its median major axis shown with gray circle.

Using equations (4–6) we estimate the brightness temperature and Doppler factor of Gc. During the flare peak  $T_{b,Gc} \approx 4 \cdot 10^{11}$  K (Figure 15). Taking the variability timescale at Gc-flare peak  $t_{var,Gc} = 0.1$  yr (estimated in the same way as for the core at flare decay in Nov 2008) and corresponding  $T_{var,Gc} = 2.4 \cdot 10^{14}$  K we obtain  $T_{b,int,Gc} \approx 10^{10}$  K,  $\delta_{Gc} \approx 24$ .

Lorentz factor and viewing angle can be estimated using the following equations:

$$\Gamma = \frac{\beta_{app}^2 + \delta^2 + 1}{2\delta}, \quad \theta = \arctan \frac{2\beta_{app}}{\beta_{app}^2 + \delta^2 - 1}, \quad (8)$$

which give  $\Gamma \approx 14$  and  $\theta \approx 1.7^\circ$ .

The slope of Gc size vs. distance from the core is  $1.2 \pm 0.4$  implying the conical angle  $\varphi_{Gc} \approx 62^\circ$ , which coincides with the opening angle  $\varphi$  obtained from the stacked image in the northern jet. The intrinsic opening angle of the jet is then  $\varphi_{int} = \varphi_{Gc} \sin \theta \approx 2^\circ$ .

If the viewing angle of the inner jet (in the core region) is the same as of Gc, then Lorentz factor and apparent speed in that region are also kept as  $\delta_{core} \approx \delta_{Gc}$ .

Since the distance between the core and Gc is less than

the beam size, one can argue that this is an artifact. However, the evolution of its size and brightness temperature with time and distance from the core (Figures 14,15) as well as its birth date suggest that Gc is a real jet component.

## 9 CORE SHIFT AND PHYSICAL PARAMETERS

Within the photosphere interpretation of the core, its apparent shift  $\Delta r$  and change of transverse size  $\Delta W_{min}$  in conical jet are related through the apparent opening angle  $\varphi$  as  $\Delta r = \Delta W_{min}/2 \tan \varphi/2$ . Here we assume that major and minor core axes are aligned with axial and transverse directions of the inner jet, which is typical for blazars (Kovalev et al. 2005).

The core shift is then can be easily found for a given frequency pair. For example, the shift between the core at 15 and 8 GHz is then  $\Delta r_{15-8} \approx 0.03$  mas, which is several times lower than the median value (0.128 mas) obtained by Pushkarev et al. (2012) for these frequencies. The smaller core shift value is expected for the source having small viewing angle. The core shift between 15 and 5 GHz is  $\Delta r_{15-5} \approx 0.1$  mas.

Estimation of physical parameters can be done taken into account the fact that the core brightness temperature is close equipartition value  $T_{b,eq} \sim 10^{10.5}$  K.

Consider standard scalings for the particles density  $N = N_1(r/r_1)^{-n}$  and magnetic field strength  $B = B_1(r/r_1)^{-m}$  (here index 1 refers to values at 1 pc from central engine).

In freely expanding jet (without ambient medium pressure) the power indexes  $m, n$  can be linked through the measured index  $k$  and spectral index  $\alpha$  (Konigl 1981)<sup>9</sup>:

$$k = \frac{5 - 2\alpha}{(3 - 2\alpha)m + 2n - 2} \quad (9)$$

Equipartition implies equality between particles and magnetic field energy density:

$$N_{1\text{pc}}(r/r_{1\text{pc}})^{-n} \gamma_{\min} m_e c^2 = K B_{1\text{pc}}^2 (r/r_{1\text{pc}})^{-2m} / 8\pi, \quad (10)$$

where  $m_e$  is the electron mass,  $\gamma_{\min}$  is the minimal Lorentz-factor of emitting electrons,  $K \approx 1/\ln(\gamma_{\max}/\gamma_{\min}) \approx 0.1$  for the maximum Lorentz-factor of emitting electrons  $\gamma_{\max} = 10^{4.34} \gamma_{\min}$  (Hirotani 2005). If this condition preserves along the jet, then  $n = 2m$ , and from (9) for  $k = 0.8$  and  $\alpha = -0.5$  we obtain  $m = 1.2$ ,  $n = 2.4$ .

The measure of core offset for a given frequency pair  $\nu_1, \nu_2$  can be introduced as (Lobanov 1998):

$$\Omega = 4.85 \cdot 10^{-9} \frac{\Delta r_{\text{mas}} D_\ell}{(1+z)^2} \left( \frac{\nu_1^k \nu_2^k}{\nu_2^k - \nu_1^k} \right), \quad (11)$$

where  $D_\ell$  is the luminosity distance in pc,  $\Delta r_{\text{mas}}$  – the core shift in mas. Then magnetic field strength at 1 pc:

$$B_1 \approx 0.014 \left( \frac{\Omega^{3/k} (1+z)^2 \ln \gamma_{\max}/\gamma_{\min}}{\delta^2 \phi \sin^{3/k-1} \theta} \right)^{1/4}, \quad (12)$$

<sup>9</sup> Note, that throughout this paper  $k$  is defined as  $k_r^{-1}$

where  $\theta$  is the jet viewing angle,  $\phi$  is the jet half opening angle and  $\delta$  is the Doppler factor. Substitution of the parameters gives  $B_1 \approx 1.3$  G. De-projected distance from the central engine to the core on a frequency  $\nu$  is then:

$$r_{\text{core}}(\nu) = \frac{\Omega}{\sin \theta} \nu^{-k} \quad (13)$$

E.g., the core at 7 mm is located at  $r_{\text{core},43} \approx 10.5$  pc, while the core at 2.3 GHz is more than 100 pc downstream the jet. The magnetic field in the 43 GHz core is then  $B_{7\text{mm core}} \approx 0.08$  G.

We assume, that the distance between the core at given two frequencies corresponds to the peak-to-peak time delay and the speed of the flow (i.e. the apparent core shift can be expressed through the delay and proper motion as  $\Delta r = \mu \Delta T$ ). For  $\Delta r_{15-5} = 0.1$  mas and  $\Delta T_{G,15-5} = 14$  days we obtain  $\mu = 2.6$  mas/yr (130c in the source redshift), which is an order of magnitude higher than the proper motion found for the Gc component. Then the bulk flow speed differs from the pattern speed in the jet of 0235+164. The high value of apparent brightness temperatures can be attributed to the high velocity of the inner jet (see Section 7.1). Probably, there is a spine-like fast and compact structure jet.

## 10 CONCLUSIONS

Application of GPR method allows us to localize the peaks of the flares with good accuracy and obtain reliable estimates of the multi-frequency time delays. Frequency dependence of the time lags and apparent core size suggest synchrotron self-absorption to dominate in the jet at the cm-mm wavelengths. Power index  $k_t$  differs significantly from one flare to another, suggesting changes in physical conditions or geometrical characteristics of the jet. The total flux profile of the 2008 flare at mm wavelengths is found to be a sum of the core and the component flux density variations. Such cases can also affect the measured difference of  $k_t$ , and must be taken into account for estimates of variability timescales, brightness temperature, Doppler factor, and core shift.

We implement a self-consistent method to estimate Doppler factor and intrinsic brightness temperature of the core using the size and variability scale of the same region. The obtained value of  $T_{b,int}$  is close to one expected in equipartition regime. The brightness temperature measured using ground-based VLBI increases by a factor 2 during the flares, but still is much lower than one obtained with the space interferometer RadioAstron, where visibility amplitudes 50 – 100 mJy are detected on bases up to 14 G $\lambda$ . Fast and compact jet regions with high Doppler factor become resolved by ground-space interferometer and show higher brightness temperatures. These spikes might demonstrate faster flux variations, which is in good agreement with the observed intra-day variability scales of 0235+164.

Doppler factor of the superluminal component Gc estimated from its kinematic analysis is in good agreement with one, found for the core from ground-based VLBA brightness temperature measurements. Estimated birth date of Gc as well as increase of its size with time and distance from the core, provide strong support for it to be a real jet component. The two prevalent directions in the scattering of the components at 7 mm are probably caused by jet bend from

south to north. The brighter, more compact and closer to the core components are observed in the southern jet during all the period studied, which provide strong support for this scenario. Also does the estimates of the opening angle of southern (from the Gc component size) and northern (from stacked image) jet. Millimeter interferometric observations with orthogonal base extension (i.e. with beam position angles  $\sim 80^\circ$ ) would shed more light on this enigmatic structure. The intrinsic opening angle of the outflow cone is close to the viewing angle within 0.7 mas of the central engine, yielding to the additional scattering of position angles of the observed components. The flow is collimated, and on larger scales ( $> 1$  mas) its opening angle becomes smaller than the viewing one. We estimate high, but not extreme values of Lorentz factor  $\Gamma = 14$  and Doppler factor  $\delta = 21$ , and moderate viewing angle  $\theta = 1.7^\circ$ .

Based on derived jet geometry we estimate the core shift magnitude in the jet of 0235+164. Within the equipartition assumption we derive gradients of magnetic field strength and electron density in the jet, as well as linear scales corresponding to the core at each frequency. Magnetic field in the 7 mm core  $B_{7\text{mm}} \approx 0.08$  G is typical reported for the blazars.

## ACKNOWLEDGMENTS

We thank Alexander Pushkarev for helpful discussion on image stacking and measuring jet opening profiles. The research was supported by Russian Science Foundation (project 16-12-10481). It makes use of 43 GHz VLBA data from the **VLBA-BU Blazar Monitoring Program** (VLBA-BU-BLAZAR; <http://www.bu.edu/blazars/VLBApject.html>), funded by NASA through the Fermi Guest Investigator Program. The VLBA is an instrument of the Long Baseline Observatory. The Long Baseline Observatory is a facility of the National Science Foundation operated by Associated Universities, Inc. The study has made use of data from the **OVRO** 40-m monitoring program (Richards et al. 2011) which is supported in part by NASA grants NNX08AW31G, NNX11A043G, and NNX14AQ89G and NSF grants AST-0808050 and AST-1109911. The **RadioAstron** project is led by the Astro Space Center of the Lebedev Physical Institute of the Russian Academy of Sciences and the Lavochkin Scientific and Production Association under a contract with the Russian Federal Space Agency, in collaboration with partner organizations in Russia and other countries.

## References

- Abraham R. G., Crawford C. S., Merrifield M. R., Hutchings J. B., McHardy I. M., 1993, *ApJ*, **415**, 101
- Agudo I., et al., 2011, *ApJ*, **735**, L10
- Ambikasaran S., Foreman-Mackey D., Greengard L., Hogg D. W., O’Neil M., 2014, preprint, ([arXiv:1403.6015](https://arxiv.org/abs/1403.6015))
- Blandford R. D., Königl A., 1979, *ApJ*, **232**, 34
- Burbidge E. M., Beaver E. A., Cohen R. D., Junkkarinen V. T., Lyons R. W., 1996, *AJ*, **112**, 2533
- Chu H. S., Baath L. B., Rantakyrö F. T., Zhang F. J., Nicholson G., 1996, *A&A*, **307**, 15
- Cohen R. D., Smith H. E., Junkkarinen V. T., Burbidge E. M., 1987, *ApJ*, **318**, 577
- Cordes J. M., Lazio T. J. W., 2002, ArXiv Astrophysics e-prints, Edelson R. A., Krolik J. H., 1988, *ApJ*, **333**, 646
- Fomalont E. B., 1999, in Taylor G. B., Carilli C. L., Perley R. A., eds, Astronomical Society of the Pacific Conference Series Vol. 180, Synthesis Imaging in Radio Astronomy II. p. 301
- Foreman-Mackey D., 2016, *The Journal of Open Source Software*, **24**
- Foreman-Mackey D., Hogg D. W., Lang D., Goodman J., 2013, *PASP*, **125**, 306
- Frey S., et al., 2000, *PASJ*, **52**, 975
- Gabuzda D. C., Cawthorne T. V., 2000, *MNRAS*, **319**, 1056
- Greisen E. W., 1990, in G. Longo & G. Sedmak ed., Acquisition, Processing and Archiving of Astronomical Images. pp 125–142
- Hastie T., Tibshirani R., Friedman J., 2009, The Elements of Statistical Learning: Data Mining, Inference, and Prediction, second edn. Springer, <http://web.stanford.edu/~hastie/ElemStatLearn>
- Hirotani K., 2005, *ApJ*, **619**, 73
- Högberg J. A., 1974, *A&AS*, **15**, 417
- Hovatta T., Valtaoja E., Tornikoski M., Lähteenmäki A., 2009, *A&A*, **494**, 527
- Johnson M. D., et al., 2016, *ApJ*, **820**, L10
- Jones D. L., Baath L. B., Davis M. M., Unwin S. C., 1984, *ApJ*, **284**, 60
- Jorstad S. G., Marscher A. P., Mattox J. R., Wehrle A. E., Bloom S. D., Yurchenko A. V., 2001, *ApJS*, **134**, 181
- Karamanavis V., et al., 2016, *A&A*, **590**, A48
- Kardashev N. S., et al., 2013, *Astronomy Reports*, **57**, 153
- Kellermann K. I., et al., 2007, *Ap&SS*, **311**, 231
- Komatsu E., et al., 2009, *ApJS*, **180**, 330
- Konigl A., 1981, *ApJ*, **243**, 700
- Kovalev Y. Y., et al., 2005, *AJ*, **130**, 2473
- Kovalev Y. Y., et al., 2016, *ApJ*, **820**, L9
- Kraus A., et al., 1999, *A&A*, **344**, 807
- Kudryavtseva N. A., Gabuzda D. C., Aller M. F., Aller H. D., 2011, *MNRAS*, **415**, 1631
- Kutkin A. M., et al., 2014, *MNRAS*, **437**, 3396
- Likhachev S. F., Kostenko V. I., Girin I. A., Andrianov A. S., Zharov V. E., Rudnitskiy A. G., 2017, preprint, ([arXiv:1706.06320](https://arxiv.org/abs/1706.06320))
- LOBANOV A. P., 1998, *A&A*, **330**, 79
- LOBANOV A., 2015, *A&A*, **574**, A84
- MacKay D. J., 2003, Information Theory, Inference and Learning Algorithms. Cambridge University Press
- Marcaide J. M., Shapiro I. I., 1984, *ApJ*, **276**, 56
- Marscher A. P., 2006, in P. A. Hughes & J. N. Bregman ed., American Institute of Physics Conference Series Vol. 856, Relativistic Jets: The Common Physics of AGN, Microquasars, and Gamma-Ray Bursts. pp 1–22, doi:[10.1063/1.2356381](https://doi.org/10.1063/1.2356381)
- Marscher A. P., 2008, in T. A. Rector & D. S. De Young ed., Astronomical Society of the Pacific Conference Series Vol. 386, Extragalactic Jets: Theory and Observation from Radio to Gamma Ray. p. 437
- Napier P. J., 1994, in Robertson J. G., Tango W. J., eds, IAU Symposium Vol. 158, Very High Angular Resolution Imaging. p. 117
- Nilsson K., Charles P. A., Pursimo T., Takalo L. O., Sillanpää A., Teerikorpi P., 1996, *A&A*, **314**, 754
- Peterson B. M., Wanders I., Horne K., Collier S., Alexander T., Kaspi S., Maoz D., 1998, *PASP*, **110**, 660
- Petrov L., Kovalev Y. Y., Fomalont E. B., Gordon D., 2011, *AJ*, **142**, 35
- Pushkarev A. B., Kovalev Y. Y., 2015, *MNRAS*, **452**, 4274
- Pushkarev A. B., Hovatta T., Kovalev Y. Y., Lister M. L.,

- Lobanov A. P., Savolainen T., Zensus J. A., 2012, [A&A](#), **545**, A113
- Pushkarev A. B., Kovalev Y. Y., Lister M. L., Savolainen T., 2017, preprint, ([arXiv:1705.02888](#))
- Pyatunina T. B., Kudryavtseva N. A., Gabuzda D. C., Jorstad S. G., Aller M. F., Aller H. D., Teräsranta H., 2007, [MNRAS](#), **381**, 797
- Qian S. J., Kraus A., Witzel A., Krichbaum T. P., Zensus J. A., 2000, [A&A](#), **357**, 84
- Rasmussen C. E., Williams C. K. I., 2005, Gaussian Processes for Machine Learning (Adaptive Computation and Machine Learning). The MIT Press
- Readhead A. C. S., 1994, [ApJ](#), **426**, 51
- Richards J. L., et al., 2011, [ApJS](#), **194**, 29
- Romero G. E., Cellone S. A., Combi J. A., 2000, [A&A](#), **360**, L47
- Shepherd M. C., 1997, in G. Hunt & H. Payne ed., Astronomical Society of the Pacific Conference Series Vol. 125, Astronomical Data Analysis Software and Systems VI. p. 77
- Sokolovsky K., 2011, PhD thesis, Max-Planck-Institut für Radioastronomie
- Sokolovsky K. V., Kovalev Y. Y., Lobanov A. P., Savolainen T., Pushkarev A. B., Kadler M., 2010b, ArXiv:1001.2591,
- Sokolovsky K. V., et al., 2010a, ArXiv:1006.3084,
- Sokolovsky K. V., Kovalev Y. Y., Pushkarev A. B., Lobanov A. P., 2011, [A&A](#), **532**, A38
- Spinrad H., Smith H. E., 1975, [ApJ](#), **201**, 275
- Stickel M., Fried J. W., Kuehr H., 1988, [A&A](#), **198**, L13
- Valtaoja E., Teräsranta H., Urpo S., Nesterov N. S., Lainela M., Valtonen M., 1992, [A&A](#), **254**, 71
- Valtaoja E., Lähteenmäki A., Teräsranta H., Lainela M., 1999, [ApJS](#), **120**, 95
- Véron-Cetty M.-P., Véron P., 2010, [A&A](#), **518**, A10
- Walker R. C., 1995, in Zensus J. A., Diamond P. J., Napier P. J., eds, Astronomical Society of the Pacific Conference Series Vol. 82, Very Long Baseline Interferometry and the VLBA. p. 247
- Webb J. R., Howard E., Benítez E., Balonek T., McGrath E., Shrader C., Robson I., Jenkins P., 2000, [AJ](#), **120**, 41
- White R. J., Peterson B. M., 1994, [PASP](#), **106**, 879
- Yang J., Gurvits L. I., Frey S., Lobanov A. P., 2008, ArXiv:0811.2926,